PHYSICAL SCIENCES

The dissipative Talbot soliton fiber laser

Heze Zhang[1], Yueqing Du[1], Chao Zeng[1], Zhipei Sun[2], Yong Zhang[3], Jianlin Zhao[1], Dong Mao[1]*

Talbot effect, characterized by the replication of a periodic optical field in a specific plane, is governed by diffraction and dispersion in the spatial and temporal domains, respectively. In mode-locked lasers, Talbot effect is rarely linked with soliton dynamics since the longitudinal mode spacing and cavity dispersion are far away from the self-imaging condition. We report switchable breathing and stable dissipative Talbot solitons in a multicolor mode-locked fiber laser by manipulating the frequency difference of neighboring spectra. The temporal Talbot effect dominates the laser emission state—in the breathing state when the integer self-imaging distance deviates from the cavity length and in the steady state when it equals the cavity length. A refined Talbot theory including dispersion and nonlinearity is proposed to accurately depict this evolution behavior. These findings pave an effective way to control the operation in dissipative optical systems and open branches in the study of nonlinear physics.

INTRODUCTION

Talbot effect, also known as Talbot self-imaging, describes the recurrence of a periodic object illuminated by a plane wave at specific planes, which was first found by Talbot (1) and then theoretically interpreted by Rayleigh (2). Hitherto, the Talbot effect has been found and applied in a myriad of fields, including Bose-Einstein condensates (3), quantum optics (4), and atom optics (5). In addition to the widely studied Talbot effect in the spatial domain, it can be extended to other domains [i.e., time (6–8), frequency (9, 10), and transverse momentum (11) domains] by virtue of the Fourier duality (12). Analogous to the spatial Talbot effect arising from the paraxial diffraction of optical beams (13), the temporal counterpart is enabled by the propagation of pulse trains in a dispersive medium under the first-order dispersion condition (7), resulting in the reconstruction of the initial periodic pulse trains (integer Talbot effect) or the revival of pulse patterns with multiplied repetition rates (fractional Talbot effect) (14). This approach can manipulate the repetition rate and intensity of pulse trains without affecting the nature of individual pulses and has been applied in temporal cloaking (15), high–repetition rate lasers (16), and waveform amplification (17).

Aided by frequency-shifted feedback, the Talbot effect has been used in single-frequency lasers to generate ultrashort pulses, known as Talbot lasers (18–20). Their longitudinal modes have a quadratic phase distribution that can be flexibly manipulated, enabling the generation of pulse trains with a controllable repetition rate based on the Talbot condition. In this case, the nonlinear effect has a negligible impact on Talbot lasers due to the relatively low pulse intensity. Apart from these linear cases, Talbot phenomena also appear in nonlinear systems (21–23). Periodic rogue waves exhibit recurrent behavior in a cubic nonlinear medium, which arises from the transverse modulation instability and the nonlinear interference of Akhmediev breathers (22).

Optical soliton originally refers to a self-organized structure that can preserve its property during propagation in conservative systems. In a lossless fiber, solitons are generated through the intricate interplay between anomalous dispersion and self-phase modulation, exhibiting the $Sech^2$ intensity profile (24). The mode-locked pulses in anomalous-dispersion fiber lasers are referred to as "solitons" because they result from the similar balance between dispersion and nonlinear effects (25). The normal-dispersion fiber lasers are capable of generating self-similar pulses and dissipative solitons. The former relies on the self-similar amplification in the gain fiber (26), while the latter depends on the balance between gain and loss (such as the filtering effect) of the system (27). All these mode-locked pulses exchange energy with the environment, and their properties vary along the cavity owing to gain, loss, dispersion, and nonlinear effects. Lately, the term "dissipative optical soliton" has gained increasing popularity to underscore the crucial role of dissipation in the formation of mode-locked pulses (28). As the typical dissipation system, the mode-locked fiber laser constitutes an ideal platform to uncover the underlying physics of nonlinear waves (27–34). Nevertheless, the temporal Talbot effect is difficult to manifest in conventional mode-locked lasers, as the longitudinal mode spacing from megahertz to gigahertz requires a dispersion value above 1000 ps^2 to satisfy the self-imaging condition (6).

Currently, synchronized multicolor mode-locked lasers were achieved by introducing spectral filter and phase modulation inside the cavity (35, 36), in which the frequency spacing of neighboring spectra lies in the terahertz range, ~10^3 times larger than that of the longitudinal modes in other laser resonators. The dispersion value required for achieving Talbot self-imaging (~1 ps^2) is comparable to the cavity dispersion, enabling the multicolor fiber laser to be an ideal platform for studying the temporal Talbot effect. In this study, we demonstrate a self-reproducible multicolor wave packet in a mode-locked fiber laser that operates in the breathing (steady) state when the integer self-imaging distance deviates from (equals) the cavity length. The formation and self-reproducing characteristics of the multicolor wave packet depend on both the Talbot effect and dissipation effect, thus leading to its designation as a dissipative Talbot soliton to emphasize their pivotal roles. A refined Talbot theory that accounts for dispersion and nonlinear effects is proposed to analytically describe the propagation of the dissipative Talbot soliton in fibers.

[1]MOE Key Laboratory of Material Physics and Chemistry Under Extraordinary Conditions, and Key Laboratory of Light Field Manipulation and Information Acquisition, Ministry of Industry and Information Technology, School of Physical Science and Technology, Northwestern Polytechnical University, Xi'an 710129, China. [2]Department of Electronics and Nanoengineering and QTF Centre of Excellence, Aalto University, Aalto, Finland. [3]National Laboratory of Solid State Microstructures, College of Engineering and Applied Sciences, and School of Physics, Nanjing University, Nanjing 210093, China.
*Corresponding author. Email: maodong@nwpu.edu.cn

RESULTS

Principle and setup

The spatial Talbot effect is interpreted as the superposition of paraxial diffraction components of a plane wave induced by a periodic structure such as grating, as shown in Fig. 1A. Because of the constructive interference of the diffracted waves, the grating image reappears at a periodic distance—Talbot length. In the temporal domain, a wave packet composed of multicolor solitons features beating fringes originating from the interference among them

(Fig. 1B, left). Such a complex wave packet resembles the light wave diffracted by the grating in the spatial domain and exhibits the Talbot self-imaging phenomenon during the propagation in dispersive medium such as single-mode fibers.

In a laser resonator with a fixed dispersion value, the self-imaging distance of a low-intensity wave packet is dependent on the frequency difference between neighboring spectra according to Talbot theory (37), similar to the spatial counterpart depending on the period of the grating. As illustrated in the right panel of Fig. 1B, when the
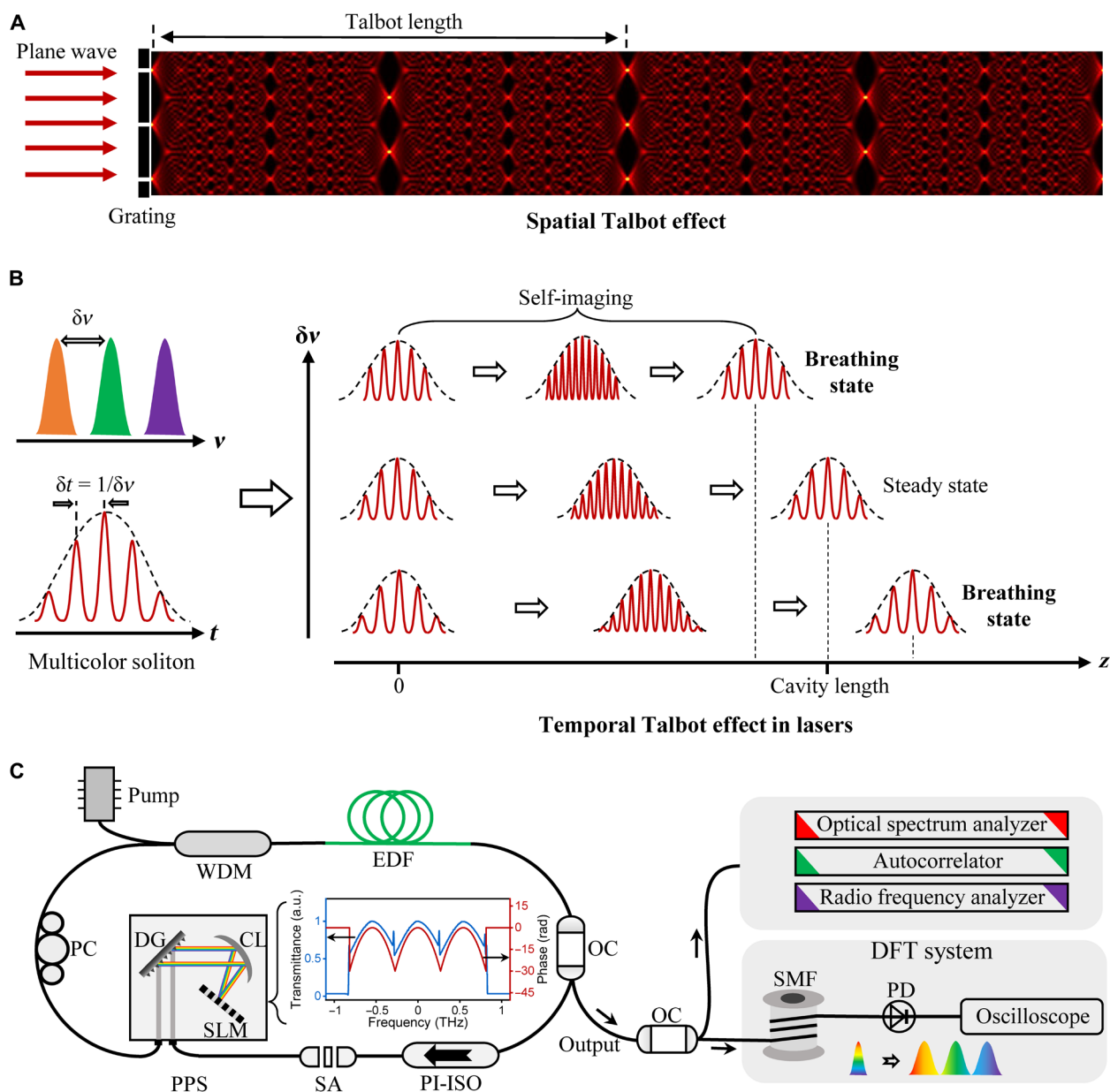
Fig. 1. Principle and setup of the dissipative Talbot soliton laser. (**A**) The spatial Talbot effect is ascribed to the interference of plane waves diffracted by a grating, manifesting as the periodic recurrence of the grating image. (**B**) In the temporal domain, the multicolor wave packet resembles these diffracted waves and exhibits recurrent phenomena during propagation in a dispersive medium. The laser operates in the breathing (steady) state when the integer self-imaging distance deviates from (equals) the cavity length. (**C**) Experimental setup. WDM, wavelength division multiplexer; EDF, erbium-doped fiber; OC, output coupler; PI-ISO, polarization-insensitive isolator; SA, saturable absorber; DG, diffraction grating; CL, cylindrical lens; SLM, spatial light modulator; PC, polarization controller; SMF, single-mode fiber; PD, photodetector; DFT, dispersive Fourier transformation; a.u., arbitrary units. The inset displays the typical spectral filter and phase modulation induced by the PPS.

integer self-imaging distance deviates from (equals) the cavity length, such a wave packet cannot (can) reproduce itself in a single round trip, generating a breathing (stable) soliton governed by the temporal Talbot effect, i.e., breathing dissipative Talbot soliton (BDTS) and stable dissipative Talbot soliton (SDTS).

We develop a synchronized multicolor soliton fiber laser to verify the above principle and explore dissipative Talbot solitons, as depicted in Fig. 1C. The cavity length and net dispersion of the fiber laser are 18.9 m and −0.52 ps^2, respectively. The programmable pulse shaper (PPS) is used within the cavity to introduce spectral filter and phase modulation in the frequency domain. When the pulse enters the PPS, it is dispersed by the diffraction grating and launched into the spatial light modulator. By manipulating the spatial light modulator with a computer, one can flexibly and precisely adjust both the transmittance and phase of each frequency as desired. The inset of Fig. 1C illustrates the typical spectral filter and phase modulation induced by the PPS, wherein the former facilitates multiwavelength lasing, while the latter partially compensates for group delay differences at these wavelengths. The parameters of the fiber laser and measurement system are given in Materials and Methods.

Before imparting spectral filtering and parabolic phase, the fiber laser delivers single-wavelength chirp-free soliton, exhibiting typical sidebands as that of the previous reports (29). By introducing periodic spectral filtering and parabolic phase with a PPS, we obtain various types of multicolor solitons in the fiber laser and study their evolution dynamics. The roles of spectral filter and phase modulation on the pulse formation are elucidated in section S1 and fig. S1. The spectral number of multicolor solitons should be no less than three to demonstrate the temporal Talbot effect. Taking the three-color soliton as an example, the frequency difference of neighboring spectra is mainly determined by the spectral filtering period, ranging from 0.493 to 0.812 THz. As the self-imaging distance mainly depends on the frequency difference of neighboring spectra, BDTSs and SDTSs can be achieved in the fiber laser by tuning the modulation period of spectral filter and parabolic phase.

Breathing dissipative Talbot solitons
A lumped propagation model is used to perform the simulations (38), in which the complex amplitude of the pulse is multiplied by the relevant matrices of each fiber component during the propagation in the laser cavity. After one round trip, the output works as the input of the next round trip until self-consistent evolution is achieved. The pulse propagation in the fiber and PPS is described by the generalized nonlinear Schrödinger equation encompassing phase modulation, spectral filtering, dispersion, nonlinearity, gain, and loss. The details of the equation and simulation parameters are illustrated in the "Simulation model" section.

We first investigate the ordinary BDTS in the simulation, which has three discrete spectra with a frequency difference of 0.764 THz. The intracavity evolution over 20 consecutive round trips is plotted in Fig. 2A, where the pulse intensity is normalized to highlight the changes in the pulse profile and beating fringe. Since the integer self-imaging distance deviates from the cavity length, the pulse changes along the cavity and reproduces itself per ~16 round trips.

Monitoring at the output coupler, the spectrum and pulse profile periodically vary with the round trip (Fig. 2, B and C). In this process, the central frequencies of the three spectra remain unchanged (Fig. 2B, right), while their intensities undergo periodic oscillations

due to the four-wave mixing effect (39). The beating fringe spacing at round trip 16 is half of that at round trip 8 (Fig. 2C, right), which is the typical characteristic of the fractional Talbot effect (16, 37). As the integer self-imaging distance differs from the cavity length, the one-half fractional image (i.e., the pulse with a halved beating fringe spacing) also appears at different cavity positions for each round trip, as can be clearly observed in Fig. 2A (e.g., the one-half fractional image appears before the output coupler for round trip 8 and at the output coupler for round trip 16). The energy of each spectrum changes with a period of 16 round trips, while the total energy varies slightly (Fig. 2D), implying a strong energy exchange governed by the four-wave mixing effect (39) and a quasi-balance between the gain and loss. The radio frequency spectrum of the ordinary BDTS displays three peaks (Fig. 2E), where the central peak corresponds to the fundamental repetition rate determined by the cavity length and the two side peaks associate with the breathing behavior.

Decreasing the modulation period to 0.532 THz while keeping other simulation parameters unchanged, we obtain another type of BDTS that exhibits a phase shift between two neighboring round trips, i.e., the inverted BDTS (Fig. 2, F to I). The spectral and energy evolutions, as well as the radio frequency spectrum, are similar to those of the ordinary BDTS, while their pulse evolutions are quite different, as marked by the white dashed box in Fig. 2G. The temporal phase shift originates from the phase difference between neighboring spectra accumulated in one round trip. The spectral phase difference is induced by the chromatic dispersion and nonlinearity of the cavity, which cannot be detected through the dispersive Fourier transform technique as it only reflects the intensity information. Such a phase shift is the typical fingerprint of the inverted temporal Talbot effect, which is similar to the spatial counterpart—the grating image at half of the Talbot length exhibits a displacement with respect to the initial grating (Fig. 1A).

Stable dissipative Talbot solitons
The temporal Talbot effect dominates the formation of the BDTS when the integer self-imaging distance deviates from the cavity length. Apart from the BDTS, the SDTS can be achieved in the same fiber laser if the integer self-imaging distance equals the cavity length. Figure 3A shows the normalized intracavity evolution of a typical SDTS with a frequency difference of 0.785 THz. Since the SDTS reproduces itself at one cavity length, the pulse profiles at the output coupler (white dashed lines) are identical for each round trip. Similar to the BDTS, we term this wave packet the ordinary SDTS due to the absence of the phase shift during pulse evolution. The details of the ordinary SDTS are illustrated in Fig. 3 (B to E), in which the spectrum, pulse profile, and normalized soliton energy are invariable with the increase of round trip. Moreover, the radio frequency spectrum (Fig. 3E) exhibits a single-peak structure, further confirming the steady state of the fiber laser.

For the spatial Talbot effect (Fig. 1A), the light field undergoes one-half fractional self-imaging twice (i.e., the grating image at one-fourth and three-fourth the Talbot length) and inverted integer self-imaging once (i.e., the grating image at one-half the Talbot length) before achieving ordinary integer self-imaging. This phenomenon can also be verified in the temporal domain by analyzing the intracavity evolution of the ordinary SDTS over two consecutive round trips (section S2 and fig. S2). From the first output coupler, the pulse profile changes three times before reaching the next output coupler,
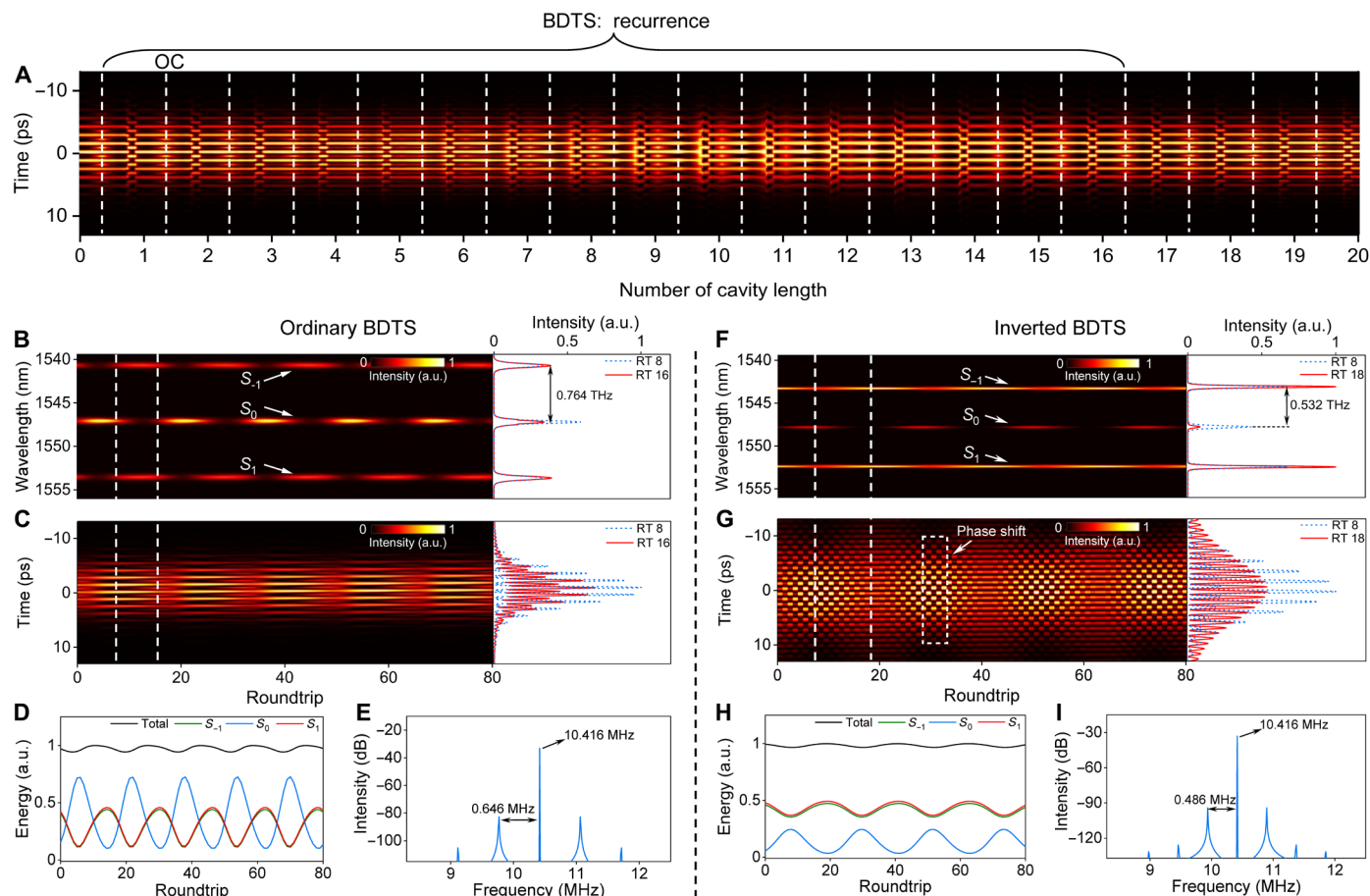
Fig. 2. BDTS in simulation. (**A**) Intracavity evolution of the ordinary BDTS over 20 consecutive round trips. Because the integer self-imaging distance deviates from the cavity length, the pulse profile at the output coupler changes with the round trip. Left: Ordinary BDTS. Right: Inverted BDTS. Evolutions of the (**B** and **F**) spectra, (**C** and **G**) pulses, and (**D** and **H**) normalized energies versus cavity round trip. (**E** and **I**) Radio frequency spectra. a.u., arbitrary units.

corresponding to one-half fractional self-imaging twice and inverted integer self-imaging once. Because of the nonuniform dispersion distribution within the laser, the self-imaging positions are not equally spaced along the laser cavity.

The SDTS also has two different forms—the ordinary SDTS and inverted SDTS. Figure 3 (F to I) shows the inverted SDTS with a frequency difference of 0.559 THz. In contrast to the ordinary SDTS, the inverted SDTS undergoes a phase shift of ~0.9 ps between neighboring round trips, i.e., the positions of the beating fringe are misaligned. As the phase shift does not affect the pulse profile and intensity, the energy of the pulse remains unchanged during the whole evolution. Moreover, the inverted SDTS only experiences one-half fractional self-imaging once between two neighboring round trips (fig. S2E), similar to the evolution of the spatial grating image within half of the Talbot length (Fig. 1A).

By using the SDTS in Fig. 3C as the input signal, we simulate the pulse evolution in lossless fibers external to the cavity (section S3 and fig. S3). The pulse exhibits the typical Talbot phenomenon during propagation, in which the one-half fractional self-imaging and integer self-imaging appear twice, similar to the pulse evolution within the laser cavity (fig. S2A). However, because of unequal group velocities among the three spectra, the pulse envelope

broadens, and the intensity decreases during further propagation in lossless fibers, indicating that the dissipative Talbot soliton cannot maintain its characteristic outside of the cavity. We further investigate the evolution of SDTS within the cavity by excluding the spectral filter, phase modulation, and dissipation effect, respectively. The pulse cannot achieve self-consistent evolution after neglecting any one of those effects, as elaborated in section S4 and fig. S4. On the basis of the above analyses, we confirm that the Talbot effect together with spectral filter, phase modulation, and dissipation effect dominate the formation of the dissipative Talbot soliton. The formation condition is much more intricate than the perturbed solitons of the nonlinear Schrödinger equation (*29*, *40*).

Experimental results
Simulations reveal the evolution behavior of the BDTS and SDTS in the same fiber laser by varying the frequency difference of neighboring spectra. Both have two types of forms, governed by either the ordinary or inverted temporal Talbot effect. To validate the simulation results, we perform an experimental study on the synchronized multicolor mode-locked fiber laser. Via changing the periodic spectral filter and phase modulation with the PPS, the BDTS and SDTS are achieved in the same fiber laser under a pump power of 24 mW.
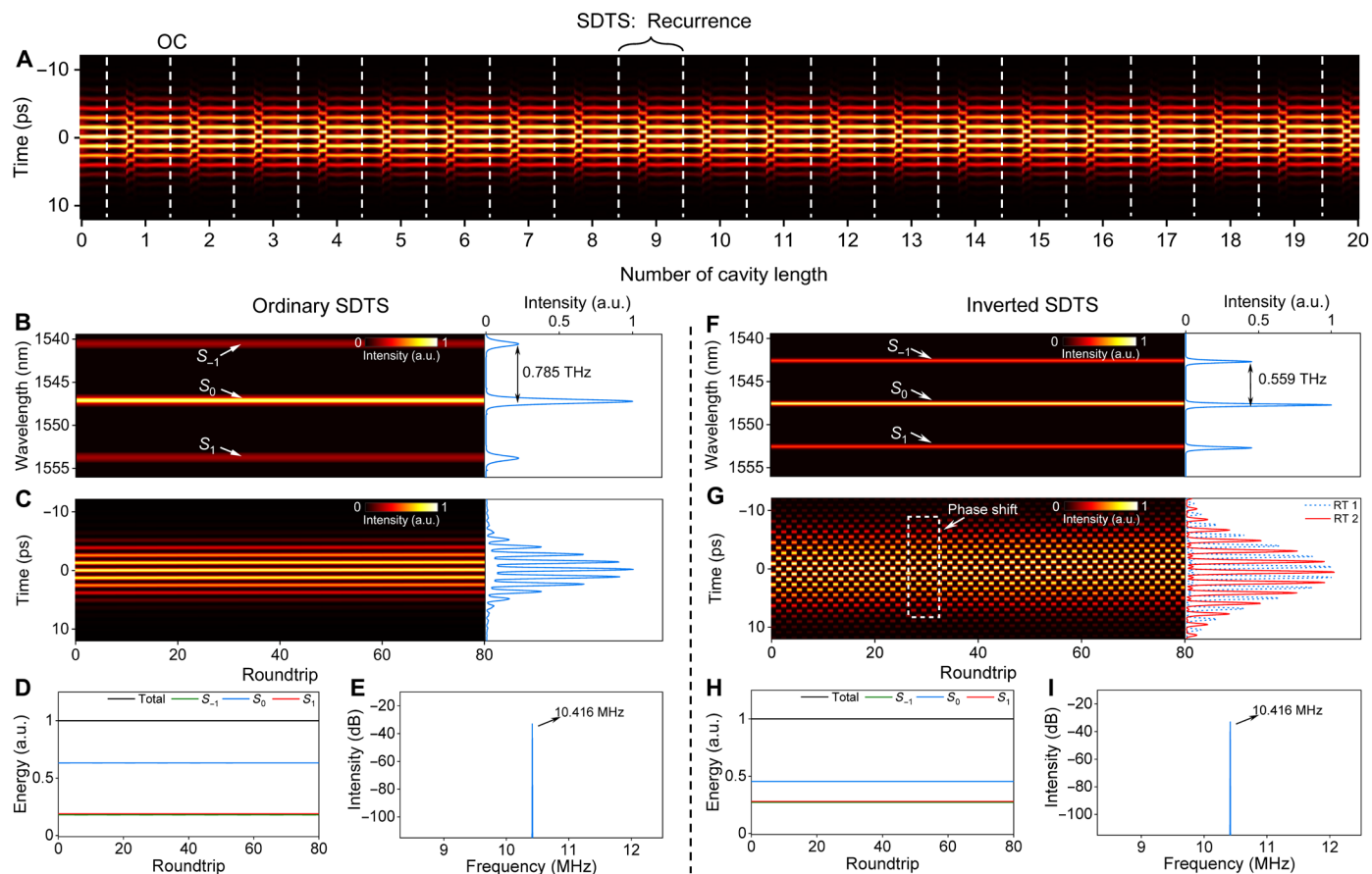
Fig. 3. SDTS in simulation. (**A**) Intracavity pulse evolution of the ordinary SDTS over 20 consecutive round trips. As the integer self-imaging distance equals the cavity length, the pulse profiles at the output coupler are identical for each round trip. Left: Ordinary SDTS. Right: Inverted SDTS. Evolutions of the (**B** and **F**) spectra, (**C** and **G**) pulses, and (**D** and **H**) normalized energies versus cavity round trip. (**E** and **I**) Radio frequency spectra. a.u., arbitrary units.

Because of the spectral filtering effect, the bandwidth of each spectrum and envelope width of the typical SDTS are about 0.5 nm and 7 ps, respectively. The corresponding time-bandwidth product is calculated to be approximately 0.4, indicating the near absence of chirp in the dissipative Talbot soliton. The formation mechanism of the dissipative Talbot soliton exhibits similarity to the pulse generated in normal-dispersion fiber lasers (*27*, *41*), as the spectral filter also plays a pivotal role in both their formation and stabilization.

Figure 4 (A to D) depicts the properties and evolution behaviors of the ordinary BDTS with a frequency difference of 0.751 THz. The measured real-time spectrum and field autocorrelation trace (Fig. 4, A and B) are consistent with the simulations. For example, the three spectra vary periodically and exchange energy with the increase of round trip, and the fractional Talbot effect can also be observed from the field autocorrelation evolution—doubled beating fringes appear per 7 round trips (Fig. 4B, right). Similar to the simulation results, the energy of each spectrum exhibits obvious oscillation with a period of 14 round trips, while the total energy remains almost unchanged with the round trip (Fig. 4C). Since the total energy remains nearly constant throughout the evolution, the BDTS is similar to the "invisible" pulsating soliton under the interplay between soliton and dispersive waves (*31*), as well as the "trampoline-like" pulsating soliton dominated by the Kerr effect and dispersion (*42*).

The ordinary SDTS can be obtained from the same fiber laser by enlarging the frequency difference to 0.778 THz (Fig. 4, E to H). Because the ordinary SDTS reproduces itself in one cavity length, the single-shot spectrum and field autocorrelation remain constant throughout the whole evolution (Fig. 4, E and F). The random energy fluctuation arises from the environmental noise and limited resolution of the dispersive Fourier transformation system (Fig. 4G). The stability of the laser is further validated by the single-peak radio frequency spectrum with a signal-to-noise ratio of ~60 dB (Fig. 4H).

In addition to the ordinary BDTS and SDTS, the fiber laser is capable of delivering the inverted BDTS and SDTS by tuning the frequency difference to 0.539 and 0.559 THz, respectively, wherein the spectrum and energy evolutions also coincide with the simulations (section S5 and fig. S5). Because the field autocorrelation trace is directly calculated from the Fourier transform of the spectral intensity (*43*), it cannot reveal the phase shift induced by the inverted temporal Talbot effect (fig. S5, B and F). A recently developed technology, known as the time lens (*44*, *45*), has emerged as a promising candidate for capturing single-shot temporal information with a subpicosecond resolution. The time lens holds great potential in accurately revealing this phase shift and completely reconstructing the real-time evolutions of the inverted BDTS and SDTS.
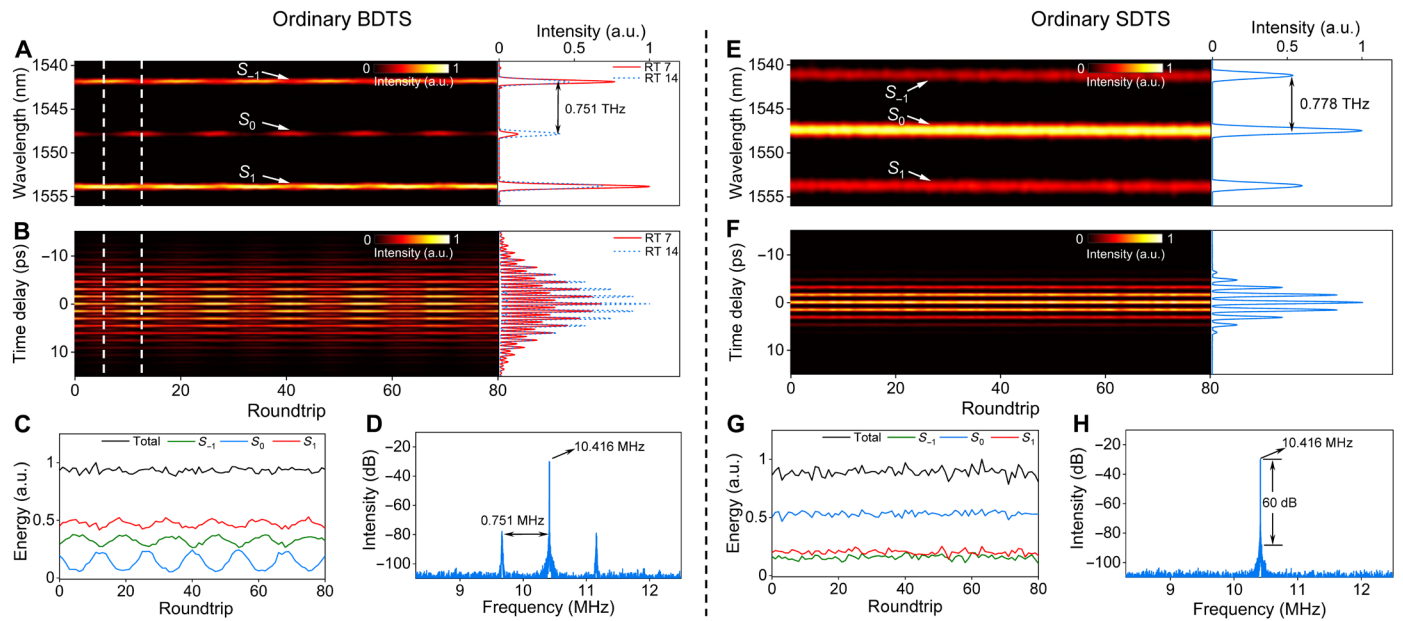
Fig. 4. Ordinary BDTS and SDTS in the experiment. Left: Ordinary BDTS. Right: Ordinary SDTS. Evolutions of the (**A** and **E**) shot-to-shot spectra, (**B** and **F**) field autocorrelations, and (**C** and **G**) normalized energies versus cavity round trip. (**D** and **H**) Radio frequency spectra. a.u., arbitrary units.

Refined Talbot theory

Both the simulation and experimental results demonstrate that the evolutions of the BDTS and SDTS are governed by the temporal Talbot effect. The laser operation (breathing or steady state) crucially depends on the relation between the integer self-imaging distance and cavity length. According to the traditional Talbot theory (*37*), the self-imaging distance is determined by the frequency difference and cavity dispersion. Such a deduction is reliable for low-intensity pulses or optical beams and has been verified by several groups in a variety of experimental configurations (*8*, *16*, *46*, *47*). Nevertheless, for pulses or beams with higher intensity, the situation becomes much more complex, as the nonlinearity cannot be ignored for the Talbot effect. For example, the self-imaging distance of periodic rogue waves increases with the pulse intensity (*22*, *48*), and the fractional image disappears for wave trains in surface gravity water under the nonlinear case (*23*).
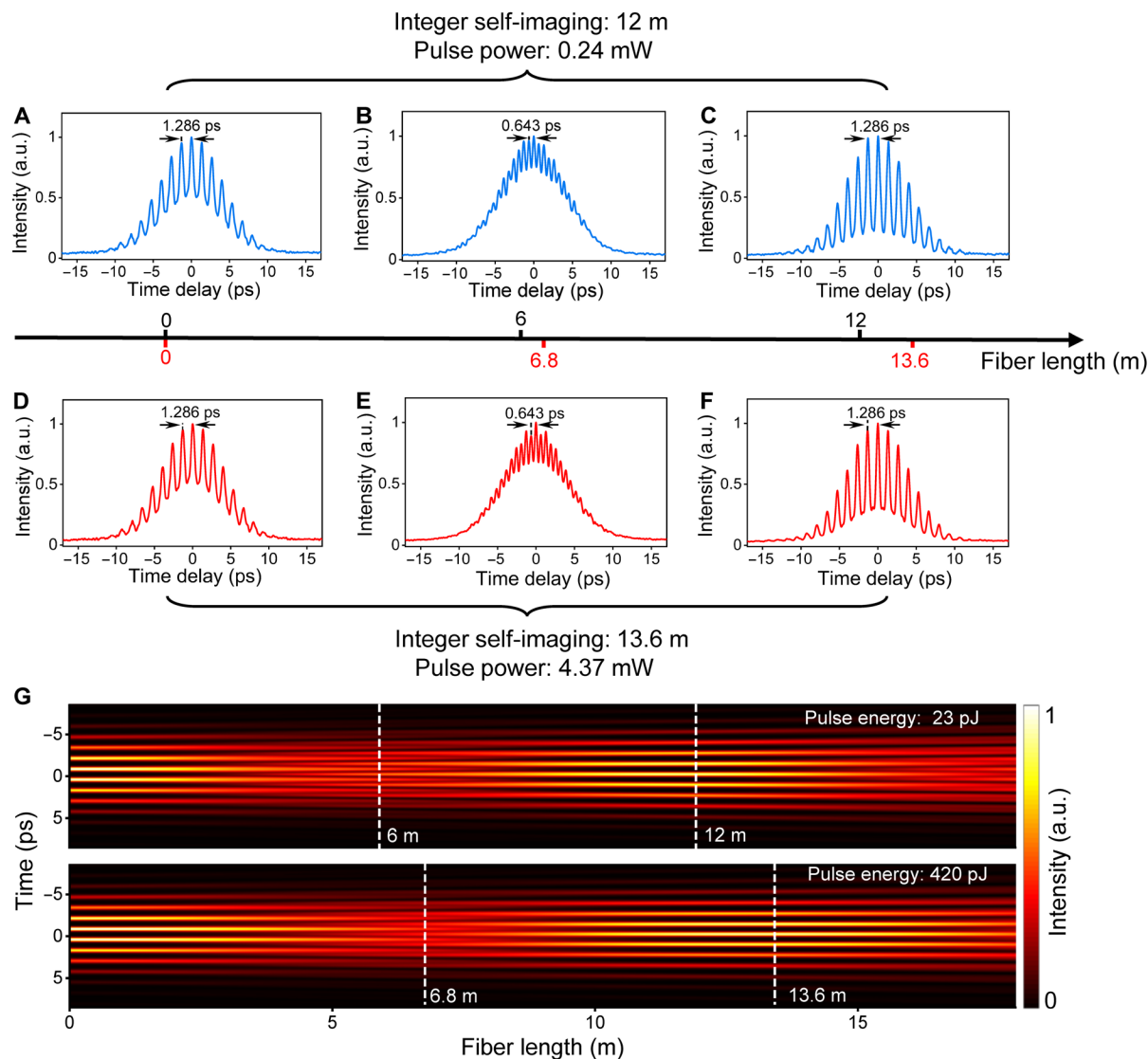
By propagating the dissipative Talbot soliton in single-mode fibers, we find that the self-imaging distance relies on both the dispersion value and pulse intensity, as illustrated in Fig. 5. The initial beating fringe spacing of dissipative Talbot soliton is measured as 1.286 ps (Fig. 5, A and D). When the pulse power is 0.24 mW, the beating fringe spacing decreases to 0.643 ps at a distance of 6 m (i.e., one-half fractional self-imaging; Fig. 5B) and returns to its initial value at a distance of 12 m (i.e., integer self-imaging; Fig. 5C), thereby confirming the presence of the Talbot effect in our laser. When the pulse power is increased to 4.37 mW, the one-half fractional and integer self-imaging distances enlarge to 6.8 and 13.6 m, respectively (Fig. 5, D to F). However, the dissipative Talbot soliton broadens and cannot achieve self-imaging at any power when the propagation length is larger than 60 m. These observations also coincide with the simulation results based on the nonlinear Schrödinger equation (Fig. 5G), further confirming that the nonlinear effect is essential for the self-imaging condition of high-intensity dissipative Talbot soliton.

For mode-locked fiber lasers, the average pulse power inside the cavity is ~3 mW. Thus, both nonlinearity and dispersion should be considered when studying the evolution of dissipative Talbot solitons. After incorporating the dispersion, self- and cross-phase modulations into Talbot theory, the phase difference ($\delta\varphi$) between the neighboring spectra can be expressed as

$$\delta\varphi = -\frac{1}{2}\beta_2 L(2\pi\nu_1 - 2\pi\nu_0)^2 + \int_0^L \gamma[P_1(z) - P_0(z)]dz \quad (1)$$

The first term on the right-hand side of Eq. 1 represents the accumulated phase difference induced by the dispersion (i.e., linear term), while the second term is the phase difference originating from the self- and cross-phase modulations (i.e., nonlinear term). β_2 is the second-order dispersion coefficient of the cavity. ν_1 and ν_0 represent the central frequencies of neighboring spectra, e.g., ν_0 for spectrum S_0 and ν_1 for spectrum S_1 (Fig. 3B). L and γ are the propagation length and cubic refractive nonlinearity of the fiber in the cavity, respectively. $P_1(z)$ and $P_0(z)$ represent the peak powers of the pulse for two neighboring spectra. In addition, the phase modulation introduced by the PPS also contributes to the linear part of $\delta\varphi$. The derivation details are given in section S6 and fig. S6.

According to refined Talbot theory, $\delta\varphi$ must be an integer multiple of π to achieve integer self-imaging. On the basis of Eq. 1, we first calculate the self-imaging distance of dissipative Talbot solitons propagating in single-mode fibers. For a lower pulse power (0.24 mW), the nonlinear term is ignorable (−0.02), and the integer self-imaging distance is calculated as 12.14 m ($\beta_2 = -21.67$ ps²/km, ν_1-$\nu_0 = 0.778$ THz, $\delta\varphi = \pi$). For a higher pulse power (4.37 mW), the nonlinear term is calculated as −0.35, giving a self-imaging distance of 13.49 m. The theoretical predictions quantitatively agree with the experimental and simulation results in Fig. 5, confirming the accuracy and reliability of the refined Talbot theory.

Fig. 5. Nonlinear propagation of dissipative Talbot solitons in single-mode fibers. Experiment: Autocorrelation traces of dissipative Talbot solitons for pulse powers of (**A** to **C**) 0.24 mW and (**D** to **F**) 4.37 mW. (**G**) Simulation results of dissipative Talbot solitons at different pulse energies. a.u., arbitrary units.

For dissipative Talbot solitons circulating in a fiber laser, we calculate $\delta\varphi$ in a single round trip versus the frequency difference ($L = 18.9$ m, $\beta_2 = -27.51$ ps^2/km), as illustrated in Fig. 6A. The gray solid line denotes the results based on traditional Talbot theory (i.e., ignoring the nonlinear term in Eq. 1), in which $\delta\varphi$ monotonically increases with the frequency difference and equals π and 2π at two discrete values. Thus, traditional Talbot theory implies that the laser should operate in the steady state for two discrete frequency differences. However, both the experiment and simulation show that the laser operates in the steady state for a wide range of parameters, which is inconsistent with the traditional Talbot theory.

For the refined Talbot theory taking the nonlinear term into account, the phase differences $\delta\varphi$ are π and 2π over a wide range of frequency differences (red dots) rather than at two discrete values, corresponding to a broad range of steady state. It is shown that both linear and nonlinear terms contribute to the self-imaging condition

of the dissipative Talbot soliton, where the nonlinear phase difference partially compensates the linear phase difference by automatically adjusting the relative intensity of each spectrum, ensuring the same value of π or 2π over a wide range of frequency differences. Physically speaking, under the combined effect of nonlinearity and saturable absorption, the fiber laser is inclined to operate in the steady state, where the dissipative Talbot soliton modifies its spectral morphology to compensate the phase difference induced by the dispersion. In this regard, the temporal Talbot effect is an attractor in nonlinear systems that displays a similar physical essence to the minimum loss principle (49).

Figure 6B shows the integer self-imaging distance of the dissipative Talbot soliton (L) as a function of the frequency difference. When the nonlinear term of Eq. 1 is ignored, the integer self-imaging distance monotonically decreases with the increase of the frequency difference (gray solid line). In comparison, the nonlinear
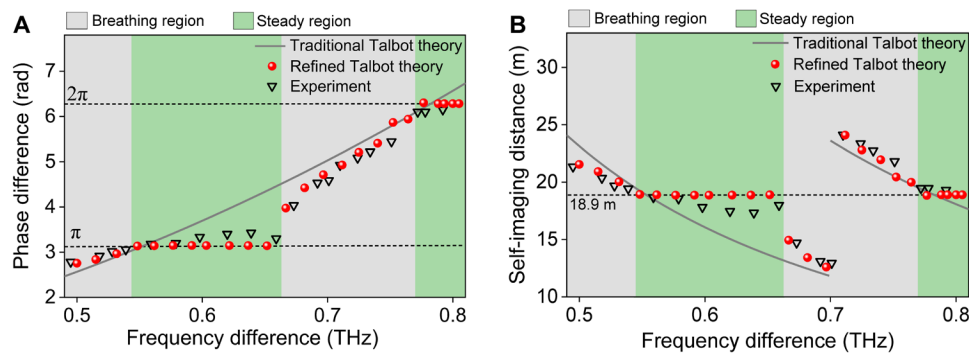
Fig. 6. Comparison between traditional Talbot theory, refined Talbot theory, and experiment. (**A**) Phase difference accumulated per round trip between neighboring spectra and (**B**) self-imaging distance versus frequency difference.

term enables the integer self-imaging distance to be comparable to the cavity length over a wide range of frequency differences. These results coincide with those in Fig. 6A, further confirming the reliability of the refined Talbot theory. In our experiment, the maximum frequency difference (0.812 THz) is limited by the effective gain bandwidth of the erbium-doped fiber, while the minimum frequency difference (0.493 THz) is mainly ascribed to the gain competition effect. Since the self-imaging distance depends on the frequency difference, we infer that the laser may switch from the steady state to the breathing state when the frequency difference is further increased.

DISCUSSION
The temporal Talbot effect shows that the dispersion value required to achieve self-imaging is inversely proportional to the longitudinal mode spacing (*37*), which limits the exploration of the Talbot wave packet in optical cavities. Here, multicolor solitons with frequency differences up to the terahertz range readily satisfy the self-imaging condition at a length comparable to the laser cavity. In this regard, the Talbot effect is not restricted to multicolor solitons, and it is also promising for exploring complex nonlinear dynamics in other ultrahigh repetition rate systems, such as microresonators (*50–54*) and four-wave mixing–induced mode-locked lasers (*55–57*). For a microresonator with a longitudinal mode spacing of 200 GHz and a dispersion value of −202 ps²/km, the integer self-imaging distance is ~20 m. Considering the cavity length of ~1 mm, the temporal Talbot effect may be responsible for breathers with thousands of periods (*58*).

In contrast to the traditional Talbot theory, nonlinear effects are considered for the refined Talbot theory to precisely describe the evolutions of the SDTS and BDTS, and this theory is also applicable to the four-color dissipative Talbot soliton (section S7 and fig. S7). Note that the spatial Talbot soliton has been demonstrated in nonlinear Kerr medium using the sinusoidal and uniform waves that are mutually coherent and trapped (*59*), in which the self-imaging distance is mainly determined by the relative phase between the input waves. However, the Talbot length in our work relies on the phase difference between neighboring spectra, encompassing both the linear and nonlinear parts. Since the nonlinear effects also contribute to the self-imaging condition, the refined Talbot theory may provide a more comprehensive interpretation of the recent reports on the

recurrent behavior of periodic rogue waves in nonlinear medium (*22, 23, 48*).

The dissipative Talbot soliton is formed in a laser system including the dispersion, nonlinearity, gain, and loss, which is similar to that of the conventional soliton (*29*), dissipative soliton (*27*), stretched pulse (*60*), and similariton (*41*). The filter-induced multiwavelength spectra together with group delay compensation between them endow the dissipative Talbot soliton with the unique ability of self-imaging, resulting in distinct evolution dynamics compared to other types of solitons. Apart from the fascinating physical mechanism, the dissipative Talbot soliton laser, with its unique synchronization property and the frequency difference of neighboring spectra lying in the terahertz range, holds great potential for applications in nonlinear optical imaging (*61–63*), difference-frequency terahertz wave generation (*64*), and laser physics (*52*).

Recent studies have successfully demonstrated the synchronization dynamics between the fundamental frequency and breathing frequency in breather lasers (*32, 65–67*). The dissipative Talbot soliton laser has a breathing frequency dominated by the Talbot effect, and further manipulation of the pump power may excite an intrinsic breathing frequency of the pulse; thus, such a laser can be an ideal platform for studying the interaction and competition among the fundamental repetition frequency, Talbot breathing frequency, and intrinsic breathing frequency.

In summary, the dissipative Talbot soliton laser, processing the multiwavelength spectra, provides an additional degree of freedom for us to explore new forms of nonlinear wave packet and uncover their evolution dynamics. By tuning the frequency difference of neighboring spectra, we found ordinary BDTS, inverted BDTS, ordinary SDTS, and inverted SDTS in the dissipative optical system. A refined Talbot theory including dispersion and nonlinear effects is proposed to precisely describe the evolution of the dissipative Talbot solitons, in which the fiber laser delivers a BDTS (SDTS) when the self-imaging distance deviates from (equals) the cavity length. From another point of view, under the coaction of nonlinearity and saturable absorption, the laser tends to operate in the steady state over a wide range of frequency differences by automatically modifying the intensity of each spectrum to compensate the phase difference induced by dispersion. These results shed light on the dynamics of solitons in nonlinear systems and open branches by combining the Talbot effect and solitons.

MATERIALS AND METHODS
Experimental setup
The synchronized multicolor mode-locked fiber laser is composed of a wavelength division multiplexer, a 6-m erbium-doped fiber (Nufern, EDFL-980-HP; $\beta_2 = 21.3$ ps^2/km), a 9:1 output coupler, a polarization-insensitive isolator, a PPS (optical path, 3.7 m; $\beta_2 = -120.3$ ps^2/km), a carbon nanotube saturable absorber, and a polarization controller. The pigtails of fiber components are single-mode fibers with length of 9.2 m (Corning, SMF-28e+; $\beta_2 = -21.7$ ps^2/km). The total length and cavity dispersion are 18.9 m and -0.52 ps^2, respectively.

Measurement system
The dissipative Talbot solitons are measured by an optical spectrum analyzer (Yokogawa, AQ6370), an autocorrelator (PulseCheck, USB-150), and a radio frequency analyzer (Agilent, E4440A). The dispersive Fourier transformation system measures the spectral evolution of the dissipative Talbot soliton, which is composed of 30-km single-mode fiber with a total dispersion of -650.1 ps^2, a 5-GHz photodetector (Thorlabs, DET09CFC/M), and a 4-GHz oscilloscope (LeCroy, 740Zi-A). On the basis of the above parameters, the overall spectral resolution of the dispersive Fourier transformation system is given as 0.26 nm (68).

Simulation model
The simulations of dissipative Talbot solitons are based on a lumped propagation model (38), in which the pulse is multiplied by the relevant matrix of each component during propagation in the laser resonator. After one circulation, the output pulse works as the input of the next round trip until the laser reaches the self-consistent state. The pulse propagation in fiber is modeled by the generalized nonlinear Schrödinger equation including dispersion, Kerr nonlinearity, gain, and loss and is solved by the symmetric split-step Fourier method (69)

$$\frac{\partial u}{\partial z} = -i\frac{\beta_2}{2}\frac{\partial^2 u}{\partial t^2} + i\gamma|u|^2 u + \frac{(g-\alpha)}{2}u + \frac{g}{2\Omega_g^2}\frac{\partial^2 u}{\partial t^2} \qquad (2)$$

where u is the slowly varying envelope of the pulse z and t represent the propagation distance and time, respectively. β_2 is the second-order dispersion coefficient, and γ is the cubic refractive nonlinearity of the fiber. g, α, and Ω_g represent the saturable gain, loss of the fiber, and gain bandwidth, respectively. $g = 0$ for single-mode fiber, and $g = g_0\exp(-E_p/E_s)$ for erbium-doped fiber, where g_0, E_p, and E_s are the small-signal gain coefficient, pulse energy, and the gain saturation energy, respectively. The saturable absorber has a transmittance $T = 0.46 - T_0/[1 + P_{(\tau)}/P_{sat}]$, where T_0 denotes the modulation depth, $P_{(\tau)}$ is the instantaneous pulse power, and P_{sat} is the saturable power.

The spectral filter and phase modulation, introduced by the PPS, are modeled by multiplying the electric field with the corresponding function in the frequency domain. The spectral filter is a periodic Gaussian function derived from the experiment. The transmittance of each period is

$$T_f(\omega) = \frac{1}{2}e^{-\frac{\ln 2(\omega-\omega_0)^2}{A^2\pi^2}} + \frac{1}{4} \qquad (3)$$

where A is the filtering bandwidth (set as 0.186 THz) and ω_0 denotes the central angular frequency of the filter.

The introduced phase is a periodic parabolic function with the same period as that of spectral filter. The phase profile of each period is $\varphi(\omega) = B(\omega - \omega_0)^2$, where B is set as -7.96 ps^2. The simulation parameters are set as follows: $E_s = 150$ pJ, $T_0 = 0.1$, and $P_{sat} = 8$ W. For the single-mode fiber, $g_0 = 0$, $\alpha = 4.6 \times 10^{-5}$/m, $\beta_2 = -21.7$ ps^2/km, $\gamma = 1.3$ W^{-1} km^{-1}. For the PPS, $\beta_2 = -120.3$ ps^2/km and $\gamma = 0$. For the erbium-doped fiber, $g_0 = 0.7$ dB/m, $\beta_2 = 21.3$ ps^2/km, and $\gamma = 3.9$ W^{-1} km^{-1}. In the simulation, the modulation periods of phase and filter can be tuned from 0.493 to 0.812 THz (3.881 to 6.312 nm) by simply changing ω_0.

Supplementary Materials
This PDF file includes:
Sections S1 to S7
Figs. S1 to S7
References

REFERENCES AND NOTES
1. H. F. Talbot, Facts relating to optical science. *Philos. Mag.* **9**, 401–407 (1836).
2. L. Rayleigh, On copying diffraction-gratings, and on some phenomena connected therewith. *Philos. Mag.* **11**, 196–205 (1881).
3. L. Deng, E. W. Hagley, J. Denschlag, J. E. Simsarian, M. Edwards, C. W. Clark, K. Helmerson, S. L. Rolston, W. D. Phillips, Temporal, matter-wave-dispersion Talbot effect. *Phys. Rev. Lett.* **83**, 5407–5411 (1999).
4. X. B. Song, H. B. Wang, J. Xiong, K. Wang, X. Zhang, K. H. Luo, L. A. Wu, Experimental observation of quantum Talbot effects. *Phys. Rev. Lett.* **107**, 033902 (2011).
5. J. Wen, S. Du, H. Chen, M. Xiao, Electromagnetically induced Talbot effect. *Appl. Phys. Lett.* **98**, 081108 (2011).
6. R. Maram, L. R. Cortes, J. Van Howe, J. Azana, Energy-preserving arbitrary repetition-rate control of periodic pulse trains using temporal Talbot effects. *J. Lightwave Technol.* **35**, 658–668 (2017).
7. T. Jannson, J. Jannson, Temporal self-imaging effect in single-mode fibers. *J. Opt. Soc. Am.* **71**, 1373–1376 (1981).
8. Y. Zhao, L. Chen, W. Wang, R. Wang, H. Hu, X. Wang, C. Zhang, W. Zhang, X. Zhang, Repetition rate multiplication control of micro-combs assisted by perfect temporal Talbot effect. *APL Photonics* **5**, 046102 (2020).
9. L. Romero Cortés, R. Maram, H. G. de Chatellus, J. Azaña, Subnoise detection and passive amplification of frequency combs through customized coherent spectral energy redistribution. *Phys. Rev. Appl.* **9**, 064017 (2018).
10. J. Azaña, Spectral Talbot phenomena of frequency combs induced by cross-phase modulation in optical fibers. *Opt. Lett.* **30**, 227–229 (2005).
11. J. Azaña, H. Guillet de Chatellus, Angular Talbot effect. *Phys. Rev. Lett.* **112**, 213902 (2014).
12. L. R. Cortes, H. Guillet de Chatellus, J. Azana, On the generality of the Talbot condition for inducing self-imaging effects on periodic objects. *Opt. Lett.* **41**, 340–343 (2016).
13. J. Wen, Y. Zhang, M. Xiao, The Talbot effect: Recent advances in classical optics, nonlinear optics, and quantum optics. *Adv. Opt. Photonics* **5**, 83–130 (2013).
14. L. Romero Cortés, R. Maram, H. G. de Chatellus, J. Azaña, Arbitrary energy-preserving control of optical pulse trains and frequency combs through generalized Talbot effects. *Laser Photon. Rev.* **13**, 1900176 (2019).
15. J. M. Lukens, D. E. Leaird, A. M. Weiner, A temporal cloak at telecommunication data rate. *Nature* **498**, 205–208 (2013).
16. R. Maram, J. Van Howe, M. Li, J. Azana, Lossless fractional repetition-rate multiplication of optical pulse trains. *Opt. Lett.* **40**, 375–378 (2015).
17. R. Maram, J. Van Howe, M. Li, J. Azana, Noiseless intensity amplification of repetitive signals by coherent addition using the temporal Talbot effect. *Nat. Commun.* **5**, 5163 (2014).
18. H. G. de Chatellus, E. Lacot, W. Glastre, O. Jacquin, O. Hugon, Theory of Talbot lasers. *Phys. Rev. A* **88**, 033828 (2013).
19. V. Billault, V. Crozatier, G. Baili, G. Feugnet, M. Schwarz, P. Nouchi, D. Dolfi, H. G. de Chatellus, Regenerative Talbot laser for generating tunable pulse train with a low phase noise. *IEEE Photonics Technol. Lett.* **31**, 1842–1845 (2019).
20. H. G. de Chatellus, O. Jacquin, O. Hugon, W. Glastre, E. Lacot, J. Marklof, Generation of ultrahigh and tunable repetition rates in CW injection-seeded frequency-shifted feedback lasers. *Opt. Express* **21**, 15065–15074 (2013).
21. Y. Zhang, J. Wen, S. N. Zhu, M. Xiao, Nonlinear Talbot effect. *Phys. Rev. Lett.* **104**, 183901 (2010).
22. Y. Zhang, M. R. Belic, H. Zheng, H. Chen, C. Li, J. Song, Y. Zhang, Nonlinear Talbot effect of rogue waves. *Phys. Rev. E* **89**, 032902 (2014).

23. G. G. Rozenman, W. P. Schleich, L. Shemer, A. Arie, Periodic wave trains in nonlinear media: Talbot revivals, Akhmediev breathers, and asymmetry breaking. *Phys. Rev. Lett.* **128**, 214101 (2022).

24. L. F. Mollenauer, R. H. Stolen, J. P. Gordon, Experimental observation of picosecond pulse narrowing and solitons in optical fibers. *Phys. Rev. Lett.* **45**, 1095–1098 (1980).

25. C.-J. Chen, P. K. A. Wai, C. R. Menyuk, Soliton fiber ring laser. *Opt. Lett.* **17**, 417–419 (1992).

26. F. Ö. Ilday, J. R. Buckley, W. G. Clark, F. W. Wise, Self-similar evolution of parabolic pulses in a laser. *Phys. Rev. Lett.* **92**, 213902 (2004).

27. P. Grelu, N. Akhmediev, Dissipative solitons for mode-locked lasers. *Nat. Photonics* **6**, 84–92 (2012).

28. K. Krupa, K. Nithyanandan, U. Andral, P. Tchofo-Dinda, P. Grelu, Real-time observation of internal motion within ultrafast dissipative optical soliton molecules. *Phys. Rev. Lett.* **118**, 243901 (2017).

29. L. E. Nelson, D. J. Jones, K. Tamura, H. A. Haus, E. P. Ippen, Ultrashort-pulse fiber ring lasers. *Appl. Phys. B* **65**, 277–294 (1997).

30. J. M. Dudley, F. Dias, M. Erkintalo, G. Genty, Instabilities, breathers and rogue waves in optics. *Nat. Photonics* **8**, 755–764 (2014).

31. M. Liu, Z. W. Wei, H. Li, T. J. Li, A. P. Luo, W. C. Xu, Z. C. Luo, Visualizing the "invisible" soliton pulsation in an ultrafast laser. *Laser Photon. Rev.* **14**, 1900317 (2020).

32. X. Wu, Y. Zhang, J. Peng, S. Boscolo, C. Finot, H. Zeng, Farey tree and devil's staircase of frequency-locked breathers in ultrafast lasers. *Nat. Commun.* **13**, 5784 (2022).

33. X. Wu, J. Peng, S. Boscolo, Y. Zhang, C. Finot, H. Zeng, Intelligent breathing soliton generation in ultrafast fiber lasers. *Laser Photon. Rev.* **16**, 2100191 (2021).

34. J. Peng, S. Boscolo, Z. Zhao, H. Zeng, Breathing dissipative solitons in mode-locked fiber lasers. *Sci. Adv.* **5**, eaax1110 (2019).

35. D. Mao, H. Wang, H. Zhang, C. Zeng, Y. Du, Z. He, Z. Sun, J. Zhao, Synchronized multi-wavelength soliton fiber laser via intracavity group delay modulation. *Nat. Commun.* **12**, 6712 (2021).

36. J. P. Lourdesamy, A. F. J. Runge, T. J. Alexander, D. D. Hudson, A. Blanco-Redondo, C. M. de Sterke, Spectrally periodic pulses for enhancement of optical nonlinear effects. *Nat. Phys.* **18**, 59–66 (2021).

37. J. Azaña, M. A. Muriel, Temporal self-imaging effects: Theory and application for multiplying pulse repetition rates. *IEEE J. Sel. Top. Quantum Electron.* **7**, 728–744 (2001).

38. D. Y. Tang, L. M. Zhao, B. Zhao, A. Q. Liu, Mechanism of multisoliton formation and soliton energy quantization in passively mode-locked fiber lasers. *Phys. Rev. A* **72**, 043816 (2005).

39. X. Xiaochuan, Y. Yong, Z. Xinhui, C. Deying, Multiple four-wave-mixing processes and their application to multiwavelength erbium-doped fiber lasers. *J. Lightwave Technol.* **27**, 2876–2885 (2009).

40. Y. S. Kivshar, B. A. Malomed, Dynamics of solitons in nearly integrable systems. *Rev. Mod. Phys.* **61**, 763–915 (1989).

41. B. Oktem, C. Ülgüdür, F. Ö. Ilday, Soliton–similariton fibre laser. *Nat. Photonics* **4**, 307–311 (2010).

42. Y. Du, C. Zeng, Z. He, Q. Gao, D. Mao, J. Zhao, Trampolinelike pulsating soliton fiber lasers. *Phys. Rev. A* **104**, 023503 (2021).

43. Z. Q. Wang, K. Nithyanandan, A. Coillet, P. Tchofo-Dinda, P. Grelu, Optical soliton molecular complexes in a passively mode-locked fibre laser. *Nat. Commun.* **10**, 830 (2019).

44. A. Tikan, S. Bielawski, C. Szwaj, S. Randoux, P. Suret, Single-shot measurement of phase and amplitude by using a heterodyne time-lens system and ultrafast digital time-holography. *Nat. Photonics* **12**, 228–234 (2018).

45. P. Ryczkowski, M. Närhi, C. Billet, J. M. Merolla, G. Genty, J. M. Dudley, Real-time full-field characterization of transient dissipative soliton dynamics in a mode-locked laser. *Nat. Photonics* **12**, 221–227 (2018).

46. L. A. Hall, M. Yessenov, S. A. Ponomarenko, A. F. Abouraddy, The space–time Talbot effect. *APL Photonics* **6**, 056105 (2021).

47. J. Wu, J. Hu, C. S. Bres, Temporal Talbot effect of optical dark pulse trains. *Opt. Lett.* **47**, 953–956 (2022).

48. Y. Zhang, M. R. Belic, M. S. Petrovic, H. Zheng, H. Chen, C. Li, K. Lu, Y. Zhang, Two-dimensional linear and nonlinear Talbot effect from rogue waves. *Phys. Rev. E* **91**, 032916 (2015).

49. L. G. Wright, P. Sidorenko, H. Pourbeyram, Z. M. Ziegler, A. Isichenko, B. A. Malomed, C. R. Menyuk, D. N. Christodoulides, F. W. Wise, Mechanisms of spatiotemporal mode-locking. *Nat. Phys.* **16**, 565–570 (2020).

50. D. C. Cole, E. S. Lamb, P. Del'Haye, S. A. Diddams, S. B. Papp, Soliton crystals in Kerr resonators. *Nat. Photonics* **11**, 671–676 (2017).

51. T. Herr, V. Brasch, J. D. Jost, C. Y. Wang, N. M. Kondratiev, M. L. Gorodetsky, T. J. Kippenberg, Temporal solitons in optical microresonators. *Nat. Photonics* **8**, 145–152 (2014).

52. T. J. Kippenberg, A. L. Gaeta, M. Lipson, M. L. Gorodetsky, Dissipative Kerr solitons in optical microresonators. *Science* **361**, (2018).

53. H. Shu, L. Chang, C. Lao, B. Shen, W. Xie, X. Zhang, M. Jin, Y. Tao, R. Chen, Z. Tao, H. Chang, S. Yu, Q. Yang, X. Wang, J. E. Bowers, Submilliwatt, widely tunable coherent microcomb generation with feedback-free operation. *Adv. Photonics* **5**, 036007 (2023).

54. Z. Sun, Y. Li, B. Bai, Z. Zhu, H. Sun, Silicon nitride-based Kerr frequency combs and applications in metrology. *Adv. Photonics* **4**, 064001 (2022).

55. W. Wang, W. Zhang, S. T. Chu, B. E. Little, Q. Yang, L. Wang, X. Hu, L. Wang, G. Wang, Y. Wang, W. Zhao, Repetition rate multiplication pulsed laser source based on a microring resonator. *ACS Photonics* **4**, 1677–1683 (2017).

56. J. Schröder, T. D. Vo, B. J. Eggleton, Repetition-rate-selective, wavelength-tunable mode-locked laser at up to 640 GHz. *Opt. Lett.* **34**, 3902–3904 (2009).

57. Z. Ding, Z. Huang, Y. Chen, C. Mou, Y. Lu, F. Xu, All-fiber ultrafast laser generating gigahertz-rate pulses based on a hybrid plasmonic microfiber resonator. *Adv. Photonics* **2**, 026002 (2020).

58. M. Yu, J. K. Jang, Y. Okawachi, A. G. Griffith, K. Luke, S. A. Miller, X. Ji, M. Lipson, A. L. Gaeta, Breather soliton dynamics in microresonators. *Nat. Commun.* **8**, 14569 (2017).

59. O. Cohen, L. Chong, T. Schwartz, T. Popmintchev, M. M. Murnane, H. C. Kapteyn, Talbot solitons. *Opt. Lett.* **33**, 830–832 (2008).

60. W. He, M. Pang, C. R. Menyuk, P. St, J. Russell, Sub-100-fs 187 GHz mode-locked fiber laser using stretched-soliton effects. *Optica* **3**, 1366–1372 (2016).

61. V. Kravtsov, S. AlMutairi, R. Ulbricht, A. R. Kutayiah, A. Belyanin, M. B. Raschke, Enhanced third-order optical nonlinearity driven by surface-plasmon field gradients. *Phys. Rev. Lett.* **120**, 203903 (2018).

62. T. Jiang, V. Kravtsov, M. Tokman, A. Belyanin, M. B. Raschke, Ultrafast coherent nonlinear nanooptics and nanoimaging of graphene. *Nat. Nanotechnol.* **14**, 838–843 (2019).

63. C. Xu, F. W. Wise, Recent advances in fibre lasers for nonlinear microscopy. *Nat. Photonics* **7**, 875–882 (2013).

64. A. Majkić, M. Zgonik, A. Petelin, M. Jazbinšek, B. Ruiz, C. Medrano, P. Günter, Terahertz source at 9.4 THz based on a dual-wavelength infrared laser and quasi-phase matching in organic crystals OH1. *Appl. Phys. Lett.* **105**, 141115 (2014).

65. D. C. Cole, S. B. Papp, Subharmonic entrainment of Kerr breather solitons. *Phys. Rev. Lett.* **123**, 173904 (2019).

66. T. Xian, L. Zhan, W. Wang, W. Zhang, Subharmonic entrainment breather solitons in ultrafast lasers. *Phys. Rev. Lett.* **125**, 163901 (2020).

67. X. Wu, J. Peng, S. Boscolo, C. Finot, H. Zeng, Synchronization, Desynchronization, and intermediate regime of breathing solitons and soliton molecules in a laser cavity. *Phys. Rev. Lett.* **131**, 263802 (2023).

68. K. Goda, B. Jalali, Dispersive Fourier transformation for fast continuous single-shot measurements. *Nat. Photonics* **7**, 102–112 (2013).

69. A. Bednyakova, S. K. Turitsyn, Adiabatic soliton laser. *Phys. Rev. Lett.* **114**, 113901 (2015).

70. G. P. Agrawal, *Nonlinear Fiber Optics* (Academic Press, 2006).